3D Path-Following using MRAC on a Millimeter-Scale Spiral-Type Magnetic Robot

Haoran Zhao[1], Julien Leclerc[1], Maria Feucht[2], Olivia Bailey[3] and Aaron T. Becker[1]

Abstract—This paper focuses on the 3D path-following of a spiral-type helical magnetic swimmer in a water-filled workspace. The swimmer has a diameter of $2.5\,\mathrm{mm}$, a length of $6\,\mathrm{mm}$, and is controlled by an external time-varying magnetic field. A method to compensate undesired magnetic gradient forces is proposed and tested. Five swimmer designs with different thread pitch values were experimentally analyzed. All were controlled by the same model reference adaptive controller (MRAC). Compared to a conventional hand-tuned PI controller, their 3D path-following performance is significantly improved by using MRAC. At an average speed of $50\,\mathrm{mm/s}$, the path-following mean error of the MRAC is $3.8\pm1.8\,\mathrm{mm}$, less than one body length of the swimmer. The versatility of this new controller is demonstrated by analyzing path-following through obstacles on a helical trajectory and forward & backward motion.

Index Terms—Medical Robots and Systems, Model Learning for Control

I. INTRODUCTION

MAGNETICALLY actuated and steered robots are promising for various biomedical applications ranging from in vitro to in vivo diagnosis and therapy [1]–[4].

In 1973, the biologist Berg found that micro-organisms such as *Escherichia coli* (*E. coli*) bacteria can swim in various liquids by rotating their helical-shaped flagella as molecular motors [5]. In 1976, Purcell showed that helical swimming is one of three main swimming methods for microorganisms in low Reynolds number (Re) environments [6]. Inspired by nature, in 1996, Honda et al. proposed the first magnetic helical-type centimeter-scale swimmer [7]. The swimmer was wirelessly driven by an external rotating magnetic field and had mobility in low Re environments. Since then, magnetically actuated micro-machines have been investigated by scientists and engineers. Representative surveys and reviews are [4], [8], [9]. Gravity compensation, mechanical design analysis, and motion control of helical robots in 2D are reported in [2], [9]–[14]. Path-following using centimeter-scale helical robots in 3D has been shown in [15], [16].

A variety of actuation methods are used for helical robots. The minimum number of magnetic sources for remote magnetic manipulation was examined in [18]. Currently,

[1]Department of Electrical & Computer Engineering, University of Houston, USA {hzhao9, jleclerc, atbecker}@uh.edu

[2]Baylor University, USA Maria_Feucht@baylor.edu

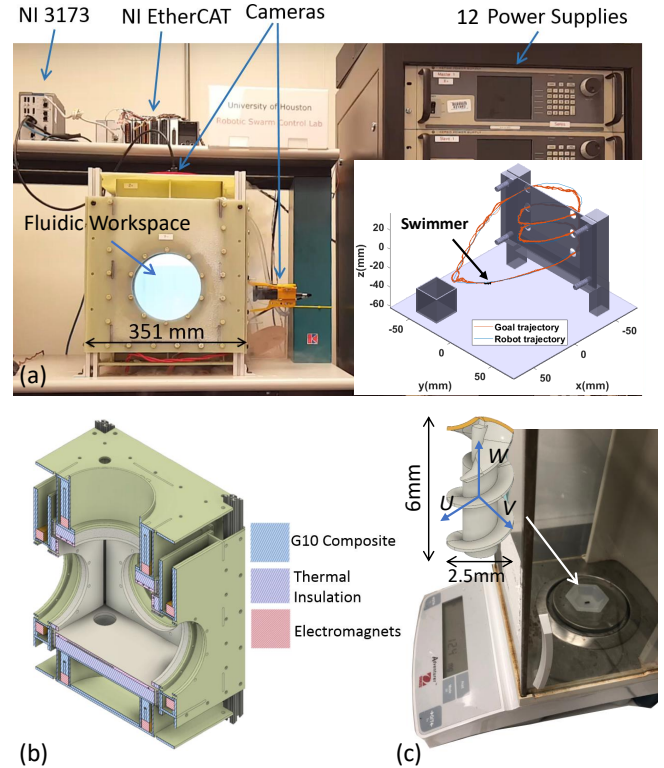[3]University of Maryland Baltimore County, USA obailey1@umbc.edu

Fig. 1. External magnetic field and spiral-type helical magnetic swimmer. The (a) experimental setup, (b) schematic cross section of the lab-built magnetic manipulator, and (c) schematic diagram of the spiral-type helical magnetic swimmer. Image (b) is from our previous paper [17].

the most common external magnetic sources are Helmholtz coils [15], [16], [19] or rotating permanent magnets as in [11], [20], [21]. Helmholtz coils produce a homogeneous magnetic field which has no gradients, but for a given maximum coil size, the workspace is smaller, and the controllable degrees of freedom is the number of coils divided by two. A five-degree-of-freedom static electromagnetic system called OctoMag was presented in [22] for controlling an untethered micro-robot in a 3D workspace. The workspace for a magnetic system is usually constrained to the enclosed volume of the coils, but systems with robotically actuated coils, such as [23], enable enlarging the workspace.

The survey [8] categorized the three base shapes for magnetically-actuated rotating robots as helix, spiral, and twist. Spiral-type magnetic swimmers have not been investigated as much as helix-shaped micro- and nano-robots, perhaps due to manufacturing challenges at those scales. Spiral-type robots are composed of magnets and a cylindrical body

with spiral-shaped fins, as shown in Fig. 1. The magnets can be the main body of the swimmer or inserted into the cylindrical body. The magnetization vector of the magnet must be perpendicular to the central axis of the cylindrical body. A torque can then be applied to rotate the swimmer and make the helical fins produce thrust; thus, swimmers can swim in fluid and agar [24]. As shown in [24], [25], because of the corkscrew-like shape, spiral-shaped micro-machines can drill through bovine tissue, which shows great potential for biomedical and in vivo applications such as blood clot removal and cyst fenestration. Also in [26], Ishiyama et al. proved that spiral-type swimmers having multiple functions can be useful for medical applications. Zhou characterized a magnetically actuated spiral-type medical robot based on an endoscopic capsule [27]. Those related works focused on spiral-type helical robots demonstrated in 2D environments or in limited channels. In [16], Wu et al. presented a helical millimeter-scale swimmer ($1.5\,\text{mm}$ diameter and $15\,\text{mm}$ length) using a radial basis function network to perform 3D path-following along arcs or straight line paths at $0.6\,\text{mm/s}$.

The present paper focuses on spiral-type swimmers with a $2.5\,\text{mm}$ diameter and $6\,\text{mm}$ length following multi-part paths at average speeds of $50\,\text{mm/s}$, as shown in Fig. 1 (c). The magnetic manipulator shown in Fig. 1 (a) and (b) was developed in our previous work [17], [28]. This coil arrangement has the advantage of providing a larger workspace than a similar-sized Helmholtz coil configuration, but the magnetic field is less uniform.

We propose a method to compensate for the gradient force applied on the swimmer when the matrix is ill-conditioned during 3D path-following. Additionally, a Model Reference Adaptive Control (MRAC) that does not require tuning was implemented for 3D path-following and compared to a conventional proportional-integrator (PI) controller. A technical solution for integrating MRAC and gradient compensation with a magnetic manipulator is presented. The method to perform inverse magnetics calculations and gradient force compensation is explained and demonstrated in Section II-A&B (using our method from [17], [28]). The Model Reference Adaptive Control for 3D path-following is described in Section II-C. Section III presents the experimental setup, results of the path-following controller comparisons, path-following performance on a helical trajectory using MRAC, and forward & backward motion. Finally, future works are discussed in Section IV.

II. METHODOLOGY

The necessary magnetics equations (II-A)-(6) were described in our previous works [17], [28]. The inverse magnetics calculation is briefly discussed based on these equations in Section II-A. Section II-B presents a method for gradient force compensation and experimental results to show the effectiveness of the method. The MRAC structure for path-following is explained in Section II-C.

A. Inverse Magnetics Calculation

A cylindrical NdFeB magnet was inserted into the swimmer such that the magnetization of the magnet is perpendicular

to the rotation axis of the swimmer. Thus, when a rotating external magnetic field is applied, the swimmer rotates to align its magnetization axis with the external magnetic field. This rotation makes the spiral-type fins produce thrust and propels the swimmer forward.

The global inertial frame of the magnetic field XYZ is defined with a right-handed coordinate system, and the origin is at the center of the workspace. A local body frame linked to the swimmer UVW is defined to simplify the calculations of the forward kinematics and inverse magnetics as shown in Fig. 1 (c); the origin is at the center of the swimmer and the W-axis is oriented perpendicular to the rotational plane of the magnetic field.

Future implementations of helical robots in 3D environments (using ultrasound or X-ray imaging) may rely on low-resolution state feedback. For this reason, the control laws and experiments in this paper only use measurements of the swimmer's 3D position. Accordingly, the two cameras in our setup only measure the swimmer's 3D position. The swimmer's magnetic orientation is not measured. Experimental observations confirm the swimmer follows the magnetic input and tracks the desired path, if the magnetic rotation frequency is below the step-out frequency of the swimmer. The control laws in this paper assume that the swimmer rotation axis aligns with the W axis and that the swimmer's magnetic orientation lags the applied magnetic field by a small amount. While this is a simplification (the two axes have small misalignments) and the lag angle is unknown, this solution has the advantage of not requiring measuring the swimmer's orientation.

The inverse magnetics equations compute the current to apply to each electromagnet (EM) to produce the desired flux density. The total flux density at any position is the sum of the flux densities produced by each of the six EM. The current vector $\mathbf{I}$ containing the currents circulating inside each EM coil is:

$$\mathbf{I} = \begin{bmatrix} I_1 & I_2 & I_3 & I_4 & I_5 & I_6 \end{bmatrix}^\top,$$

The flux density is calculated using the following equations:

$$\mathbf{B}_{xyz}(\mathbf{P}) = \begin{bmatrix} \tilde{\mathbf{B}}_{x(\mathbf{P})} \\ \tilde{\mathbf{B}}_{y(\mathbf{P})} \\ \tilde{\mathbf{B}}_{z(\mathbf{P})} \end{bmatrix} \cdot \mathbf{I} = \mathbf{A}_B(\mathbf{P}) \cdot \mathbf{I}, \qquad (1)$$

where $\mathbf{B}_{xyz}(\mathbf{P})$ is the total flux density at position $\mathbf{P}$.

$$\tilde{\mathbf{B}}_{x(\mathbf{P})} = \begin{bmatrix} \tilde{B}_{1x(\mathbf{P})} & \tilde{B}_{2x(\mathbf{P})} & \tilde{B}_{3x(\mathbf{P})} & \tilde{B}_{4x(\mathbf{P})} & \tilde{B}_{5x(\mathbf{P})} & \tilde{B}_{6x(\mathbf{P})} \end{bmatrix},$$
$$\tilde{\mathbf{B}}_{y(\mathbf{P})} = \begin{bmatrix} \tilde{B}_{1y(\mathbf{P})} & \tilde{B}_{2y(\mathbf{P})} & \tilde{B}_{3y(\mathbf{P})} & \tilde{B}_{4y(\mathbf{P})} & \tilde{B}_{5y(\mathbf{P})} & \tilde{B}_{6y(\mathbf{P})} \end{bmatrix},$$
$$\tilde{\mathbf{B}}_{z(\mathbf{P})} = \begin{bmatrix} \tilde{B}_{1z(\mathbf{P})} & \tilde{B}_{2z(\mathbf{P})} & \tilde{B}_{3z(\mathbf{P})} & \tilde{B}_{4z(\mathbf{P})} & \tilde{B}_{5z(\mathbf{P})} & \tilde{B}_{6z(\mathbf{P})} \end{bmatrix}.$$

where $\tilde{B}_{ia(\mathbf{P})}$ corresponds to the flux density produced per unit of current (T/A) by electromagnet i along the a-axis where a is x, y, or z. The coefficients $\tilde{B}_{ia(\mathbf{P})}$ are derived from the Biot-Savart law as calculated in [29].

The gradient force $\mathbf{F}_{xyz}(\mathbf{P})$ is calculated with:

$$\mathbf{F}_{xyz}(\mathbf{P}) = \begin{bmatrix} F_{x(\mathbf{P})} \\ F_{y(\mathbf{P})} \\ F_{z(\mathbf{P})} \end{bmatrix} = \nabla(\mathbf{m} \cdot \mathbf{B}_{xyz(\mathbf{P})}), \qquad (2)$$

where $F_{a(\mathbf{P})}$ is the force at Position $\mathbf{P}$ along a-axis, $\mathbf{m}$ is the swimmer's magnetization vector. m_a, shown below, is the magnetization along a-axis. Equation (2) can be rewritten as:

$$\mathbf{F}_{xyz}(\mathbf{P}) = \begin{bmatrix} m_x \frac{\partial \tilde{\mathbf{B}}_{x(\mathbf{P})}}{\partial x} + m_y \frac{\partial \tilde{\mathbf{B}}_{y(\mathbf{P})}}{\partial x} + m_z \frac{\partial \tilde{\mathbf{B}}_{z(\mathbf{P})}}{\partial x} \\ m_x \frac{\partial \tilde{\mathbf{B}}_{x(\mathbf{P})}}{\partial y} + m_y \frac{\partial \tilde{\mathbf{B}}_{y(\mathbf{P})}}{\partial y} + m_z \frac{\partial \tilde{\mathbf{B}}_{z(\mathbf{P})}}{\partial y} \\ m_x \frac{\partial \tilde{\mathbf{B}}_{x(\mathbf{P})}}{\partial z} + m_y \frac{\partial \tilde{\mathbf{B}}_{y(\mathbf{P})}}{\partial z} + m_z \frac{\partial \tilde{\mathbf{B}}_{z(\mathbf{P})}}{\partial z} \end{bmatrix} \cdot \mathbf{I},$$

$$\mathbf{F}_{xyz}(\mathbf{P}) = \mathbf{A}_F(\mathbf{P}) \cdot \mathbf{I} \qquad (3)$$

The current needed to produce the desired flux density on the swimmer can be calculated by inverting (1). The matrix $\mathbf{A}_B(\mathbf{P}) \in \mathbb{R}^{3 \times 6}$ in (1) is called the actuation matrix of flux density and the matrix $\mathbf{A}_F(\mathbf{P}) \in \mathbb{R}^{3 \times 6}$ in (3) is called the actuation matrix of force. The system is under determined and has an infinite number of solutions. Because both actuation matrices have linearly independent rows, the right Moore-Penrose pseudoinverse is performed to find a solution:

$$\mathbf{A}^+ = \mathbf{A}^* \left(\mathbf{A} \cdot \mathbf{A}^* \right)^{-1}, \qquad (4)$$

where $\mathbf{A}$ is an actuation matrix. $\mathbf{A}^+$ and $\mathbf{A}^*$ are defined as the inverse and conjugate transpose of the matrix. The desired current can be computed by substituting the inversed $\mathbf{A}_B(\mathbf{P})$ using (4) into (1).

The power $P_{\mathbf{L}}$ lost in the system via Joule heating can be calculated as $P_{\mathbf{L}} = R \cdot \|\mathbf{I}\|^2$, where R is the electric resistance of the EMs and $\|\mathbf{I}\|$ is the Euclidean norm of the current vector. The losses are proportional to $\|\mathbf{I}\|^2$. The Moore-Penrose pseudo inverse returns the solution that minimizes the Euclidean norm of the current vector and therefore minimizes the power lost via Joule heating [22].

B. Gradient Force Compensation

In our previous work [28], only the magnetic flux density was controlled through the least squares solution of (1). This solution produces a non-zero gradient in the general case, and the force produced by the gradient was neglected. As in [17], the actuation matrix is selected as (5) to reduce the effect of the undesired gradient force:

$$\mathbf{A}_{BF}(\mathbf{P}) = \begin{bmatrix} \tilde{\mathbf{B}}_{x(\mathbf{P})} \\ \tilde{\mathbf{B}}_{y(\mathbf{P})} \\ \tilde{\mathbf{B}}_{z(\mathbf{P})} \\ m_x \frac{\partial \tilde{\mathbf{B}}_{x(\mathbf{P})}}{\partial x} + m_y \frac{\partial \tilde{\mathbf{B}}_{y(\mathbf{P})}}{\partial x} + m_z \frac{\partial \tilde{\mathbf{B}}_{z(\mathbf{P})}}{\partial x} \\ m_x \frac{\partial \tilde{\mathbf{B}}_{x(\mathbf{P})}}{\partial y} + m_y \frac{\partial \tilde{\mathbf{B}}_{y(\mathbf{P})}}{\partial y} + m_z \frac{\partial \tilde{\mathbf{B}}_{z(\mathbf{P})}}{\partial y} \\ m_x \frac{\partial \tilde{\mathbf{B}}_{x(\mathbf{P})}}{\partial z} + m_y \frac{\partial \tilde{\mathbf{B}}_{y(\mathbf{P})}}{\partial z} + m_z \frac{\partial \tilde{\mathbf{B}}_{z(\mathbf{P})}}{\partial z} \end{bmatrix} \quad (5)$$

Here m_a is the magnetization vector along a-axis. Thus, the flux density and force are equal to:

$$\begin{bmatrix} \mathbf{B}_{xyz}(\mathbf{P}) \\ \mathbf{F}_{xyz}(\mathbf{P}) \end{bmatrix} = \mathbf{A}_{BF}(\mathbf{P}) \cdot \mathbf{I}. \qquad (6)$$

One way to minimize the gradient force produced with the desired current is to set the forces equal to zero in the left term of (6). Because the actuation matrix $\mathbf{A}_{BF}(\mathbf{P})$ is ill-conditioned, it can saturate the control input, cause $\mathbf{I}$ to oscillate rapidly, and trigger the safety protection of the power
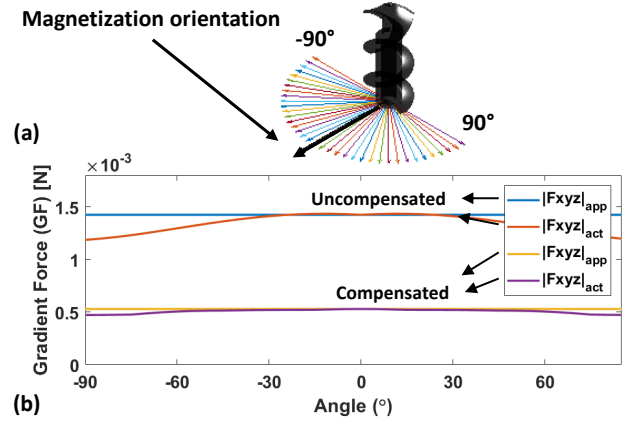

Fig. 2. Numerical study on the effect of angle between actual swimmer magnetization and approximated swimmer magnetization on the maximum gradient force of the simulated workspace. Acronyms: "app" is "approximated"; "act" is "actual."

supplies. To fix this problem, Tikhonov regularization was implemented. As described in [30], if there are zero eigenvalues, the matrix is impossible to invert. As eigenvalues approach zero, the matrix tends toward rank-deficiency, and inversion becomes less stable. Tikhonov regularization suppresses the influence of small eigenvalues in computing the inverse, filtering out the undesired components. The pseduoinverse (4) with Tikhonov regularization can be rewritten as:

$$\mathbf{A}_{\mathbf{BF}}^+(\mathbf{P}) = \mathbf{A}_{\mathbf{BF}}^*(\mathbf{P}) \left(\mathbf{A}_{\mathbf{BF}}(\mathbf{P}) \cdot \mathbf{A}_{\mathbf{BF}}^*(\mathbf{P}) + \Gamma \cdot \Gamma^* \right)^{-1},$$

where $\Gamma = \alpha \mathbb{I}$, α scales the regularization, and $\mathbb{I}$ is a identity matrix. For our setup, $\mathbb{I} \in \mathbb{R}^{6 \times 6}$ and $\alpha = 10^{-7}$ was selected so that $\mathbf{A}_{\mathbf{BF}} \cdot \mathbf{A}_{\mathbf{BF}}^*$ and $\Gamma \Gamma^*$ have the same order of magnitude. The magnitude of α is small because the computations are in meters (10^3 millimeter) and tesla (10^3 millitesla).

The magnetization vector of the swimmer was approximated as a vector perpendicular to the heading of the control signal. A numerical study on the gradient force was performed to analyze the effect of approximating the swimmer magnetization orientation. To simplify the numerical study in a 3D workspace, the desired flux density vector and swimmer magnetization vector were set to match the black arrow in Fig. 2 (a). Below the step-out frequency, the angle difference between the swimmer's magnetization and the external magnetic field is less than $90°$, so the angle range in this numerical study is $[-90°, 90°]$. The coil currents were computed once using the approximated magnetization vector, while $\mathbf{A}_{\mathbf{F}}(\mathbf{P})$ was calculated over the full $[-90°, 90°]$ range. This study simulated a $2\,\text{mT}$ magnetic field, and computed a total of 12.5×10^4 points in a $0.15\,\text{m}$ cube workspace. As shown in Fig. 2 (b), the magnitude difference for the uncompensated gradient force between approximated and actual is about 8%, and the magnitude difference for the compensated gradient force between approximated and actual is about 5%.

To experimentally demonstrate the proposed method, the PI controller from our previous work was implemented [17], [28]. The approximated gradient force $\mathbf{F}_{xyz}(\mathbf{P})$ was computed during 3D path-following. The desired circle trajectories used
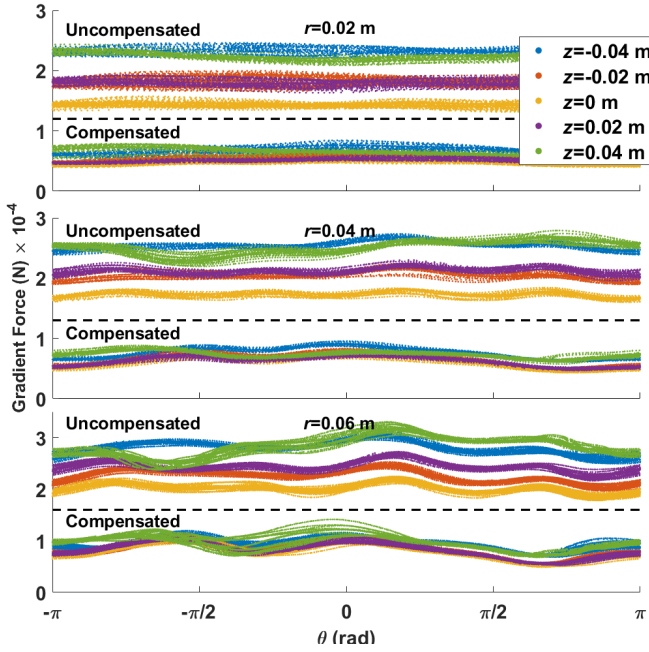
Fig. 3. Gradient force along a circular path. The figures present the uncompensated and compensated gradient force of 3 radii (0.02 m, 0.04 m, and 0.06 m) magnitude of circle trajectory and 5 z-axis magnitudes (0 m, ± 0.02 m, and ± 0.04 m).

in the experiments have five z-axis magnitudes (0 m, ± 0.02 m, and ± 0.04 m) and three radii magnitudes (0.02 m, 0.04 m, and 0.06 m). For each of these 15 cases, 10 trials were conducted. In Fig. 3, the uncompensated force is plotted for five z-axis magnitudes and for three radii (upper layer of each subplot). The compensated force values are presented in the lower layer of each subplot. As shown as Fig. 3, the uncompensated force is symmetric about the z-axis. Because the mass of the swimmer is 12.4 mg and the weight is 1.22×10^{-4} N, the magnitude of the uncompensated force ranges from 1.2 to 2.6 times the gravity force on the swimmer. Moreover, it increases when the radius of the circle trajectory increases because larger circle trajectories are closer to the EM. After implementing the Tikhonov regularization, the pseudo gradient force applied on the swimmer along the path-following trajectories ranges from 0.5 to 0.9 times the gravitational force on the swimmer. In practice, perhaps due to poor estimates of the dipole orientation, this compensation had a modest effect, reducing on average the tracking error by 28% of the uncompensated error for $z = 0.04$ m and reducing the error's standard deviation by 41%. While this compensation was computationally efficient to implement, the path following was only modestly improved, so the rest of the experiments in this paper do not use gradient compensation.

C. Direct Model Reference Adaptive Control (MRAC)

Our previous work used a PI controller to guide the swimmer in a 3D environment [17], [28]. To improve the tracking mean error and standard deviation, that controller used a feed-forward component to compensate for the acceleration of gravity and drag. However, to control the swimmer and track its trajectory in 3D, the swimmer mass, thrust coefficient

and drag coefficients were hand-tuned by a trial-and-error approach.

In contrast, the direct MRAC is a technique used for adjusting an unknown time-variant or time-invariant plant in real-time to regulate the plant to the desired system dynamics. The desired system dynamics is called the reference system (or model). Because our system is a nonlinear time-variant system, MRAC addresses the robustness issues of nonlinearity and model uncertainty without approximating the dynamic or kinematic parameters. Demonstrations and analysis of direct MRAC performance on a nonlinear system are presented in [31]. Also, the simulations and experiments in [32], [33], proved that a MRAC controller can provide a better convergence speed and tracking performance than a PI controller. The adaptive adjustment mechanism of MRAC can be derived from the rules developed in [34] or a candidate Lyapunov function [35]. The general MRAC structure is shown as following, and the system plant is defined as:

$$\dot{x}_p(t) = A_p x_p(t) + B_p u_p(t),$$
$$y_p(t) = C_p x_p(t),$$

where A_p, B_p, C_p are the state-space matrix of the plant, and $x_p(t), y_p(t), u_p(t)$ are the states, output and input of the plant. The reference model is defined as:

$$\dot{x}_m(t) = A_m x_m(t) + B_m u_m(t),$$
$$y_m(t) = C_m x_m(t),$$

where A_m, B_m, C_m are the state-space matrix of the reference model, A_m is a Hurwitz matrix (the spectrum of A_m is composed of eigenvalues with negative real parts). $x_m(t), y_m(t)$ are the states, output of the reference model, and $u_m(t)$ is the trajectory input for the reference model.

In this paper, the MRAC algorithm is derived based on the Command Generator Tracker (CGT) from [31]. The derivation and stability analysis of the adaptive controller is presented and demonstrated in [31]. The control diagram is shown in Fig. 4 (b).

$$r(t) = \begin{bmatrix} e_y(t) \\ x_m(t) \\ u_m(t) \end{bmatrix}, \tag{7}$$
$$K(t) = K_a(t) + K_n(t) \qquad \text{or equivalently,} \tag{8}$$
$$K(t) = \begin{bmatrix} K_e(t), K_x(t), K_u(t) \end{bmatrix}, \tag{9}$$
$$u_p(t) = K(t)r(t), \tag{10}$$

The adaptive controller is defined by equations (7) to (10), where $r(t)$ is the input of the adaptive adjustment mechanisms, $e_y(t) \triangleq y_m(t) - y_p(t)$, and $K(t)$ is the sum of the adaptive gains $K_a(t)$ and the nominal gains $K_n(t)$ as (8), which can also be represented by gains for each state in $r(t)$ as (9). Finally, the system input is state feedback on $r(t)$ as (10). The adaptive adjustment mechanisms of $K(t)$ are:

$$\dot{K}_a(t) = (y_m(t) - y_p(t)) r^T(t) \Upsilon, \qquad \Upsilon > 0 \tag{11}$$
$$K_n(t) = (y_m(t) - y_p(t)) r^T(t) \bar{\Upsilon}, \qquad \bar{\Upsilon} > 0. \tag{12}$$

Here Υ and $\bar{\Upsilon}$ should be positive definite and positive semidefinite adaption coefficient matrices. In this work, $\Upsilon = \bar{\Upsilon} =$
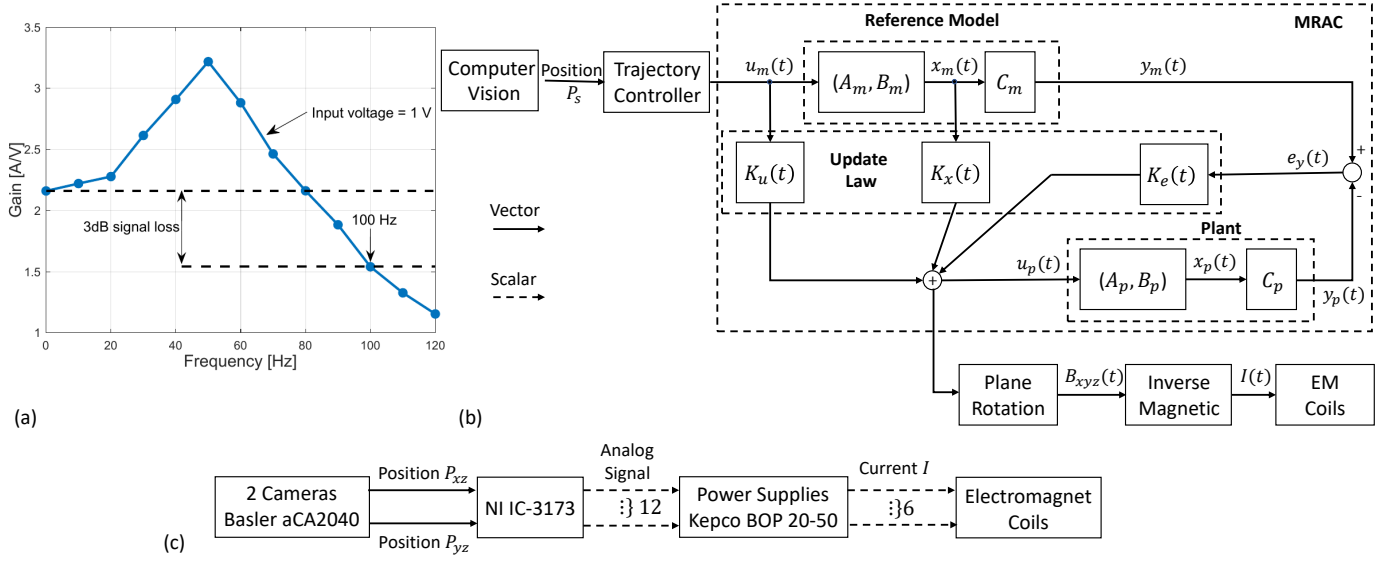
Fig. 4. System overview: (a) Identifying the band-pass frequency of one coil. (b) Control system block diagram. (c) Hardware system block diagram.

$10\mathbb{I}_3$. The magnetic swimmer system exhibits overshoot and damping, so a second-order system was selected as the reference model for each degree of freedom. Thus, the reference model's A_m and B_m are defined as:

$$A_m = \begin{bmatrix} 0 & \mathbb{I}_3 \\ -\omega_n^2\mathbb{I}_3 & -2\omega_n\zeta\mathbb{I}_3 \end{bmatrix},$$
$$B_m = \begin{bmatrix} 0 & \omega_n^2\mathbb{I}_3 \end{bmatrix}^T,$$

where $\mathbb{I}_n$ is the identity matrix of size n. The state of the reference model x_m is:

$$x_m = \begin{bmatrix} X_m & Y_m & Z_m & \dot{X}_m & \dot{Y}_m & \dot{Z}_m \end{bmatrix}^T,$$

where X_m, Y_m, and Z_m are displacements along each axis, and $\dot{X}_m$, $\dot{Y}_m$, and $\dot{Z}_m$ are the velocity along each axis. The plant has the same states as the reference model. The position information can be gained by the top and right-side cameras, and the velocity can be approximated by the change in the position measurements multiplied by the frame rate. The damping ratio of the reference model is selected to be critically damped ($\zeta = 1$), with natural frequency $\omega_n = 5\,\text{rad s}^{-1}$, yielding a 90% rise time of about 0.8 sec. The selected parameters ($\Upsilon, \bar{\Upsilon}, \zeta, \omega_n$) were chosen through a trial-and-error approach seeking to minimize the mean tracking error.

III. EXPERIMENTAL SETUP AND RESULTS

The closed-loop experiments presented in this paper include three parts: (1) stability studies on swimmer pitch, (2) controller comparison between PI controller and MRAC, and (3) following helical and back-and-forth paths.

A. Experimental Setup

The magnetic manipulator is a lab-built robotic system able to control miniature swimmers in 3D [17], [28]. A picture
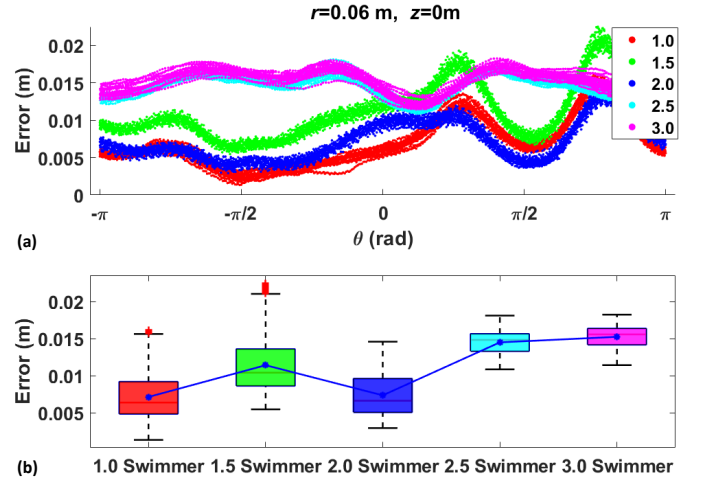

Fig. 5. Path-following results of swimmers using PI control. (a) Path-following error as a function of angle around the circle. (b) Box and whisker plots of the average error for each swimmer. Each box and whisker marker represents 15 circular laps.

of the magnetic manipulator system is shown in Fig. 1. It produces a magnetic field to apply a torque and/or a force on a magnetic object. The desired flux density, force, and torque can be controlled in 3D using the inverse magnetics calculation described in Section II. The water-filled, cube-shaped workspace for the spiral-type swimmer is designed with a side length of $150\,\text{mm}$ and placed in the center of the manipulator. The external magnetic field is generated via three pairs of electromagnetic coils placed along the xyz-axes. The electromagnet pairs are placed on opposite sides along the same axis and are separated by $300\,\text{mm}$. Current-mode power supplies are used to power the whole system. In this mode, each power supply internally performs a current regulation. Controlling the current rather than the voltage is preferred because the magnitude of the produced magnetic

field is proportional to the current. Moreover, the magnetic field has the same frequency as the current. As shown in Fig. 4 (a), the band-pass of the magnetic system is about 100 Hz, where the output drops by -3dB. Each coil is connected to a set of two Kepco BOP $20 - 50$ ($20\,\text{A}$, $50\,\text{V}$) power supplies connected in series. The whole power system can provide $20\,\text{A}$ and $100\,\text{V}$ to each coil ($12\,\text{kW}$ total power), and a National Instruments (NI) Ethercat input/output interface produces six analog outputs to control the power supplies. A thermocouple was attached to each electromagnet to detect overheating. An NI industrial controller IC 3173 is used as the system processor. Two Basler aCA2040 cameras are placed on two orthogonal sides of the workspace and measure the position of swimmers in 3D at 350-400 frames per second. The measurements from the two cameras are used as feedback for closed-loop control. The system hardware diagram is shown in Fig. 4 (c).

For the experimental studies presented in the following sections, the swimmer moved in a workspace filled with water. Compared to nano or micro helical robots which swim at low Reynolds number (Re $\leq 10^{-3}$), our millimeter-scale spiral-type swimmer is designed to swim at relatively high Re environment (e.g., for this case, $\mathbf{Re}_{\text{water}} \approx 727$). All swimmer designs presented in Table I are 3D-printed by a ProJet 3510 HD Printer. The length and diameter of all swimmers are $6\,\text{mm}$ and $2.5\,\text{mm}$.

B. Experimental Results

1) Stability Studies: To explore how design affects swimming stability, five thread-pitch values were experimentally studied. The "stability" is evaluated by the mean and standard deviation (std) of path-following error. Lower mean path-following error corresponds with better stability. All swimmers were controlled by a PI controller to follow a desired circle trajectory with z-axis $= 0\,\text{mm}$, radius $= 60\,\text{mm}$, which is at the center of the workspace, and a $68\,\text{Hz}$ rotating frequency. The pitches of the swimmers (shown in Table I) vary from $1\,\text{mm}$ to $3\,\text{mm}$ with $0.5\,\text{mm}$ intervals. 15 trials were conducted for each design. The path-following tracking error as a function of angular progress around the circle is shown in Fig. 5 (a). From the box and whisker plot shown in Fig. 5 (b), the 2.0 Swimmer had the best stability (mean $7.4\,\text{mm}$, std $= 2.7\,\text{mm}$), and the 3.0 Swimmer had the worst stability (mean$= 15.4\,\text{mm}$, std $= 1.5\,\text{mm}$).

2) Controller Comparison: To better control and guide the spiral-type swimmer in a 3D environment, a direct model reference adaptive controller (MRAC) was implemented. In this section, we experimentally compared path-following performance using PI controller and MRAC using both the best and the worst swimmers. The rotation frequency of both experiments is set as a constant value of $68\,\text{Hz}$. The radius of the desired circle trajectory is $60\,\text{mm}$, and the magnitude of z-axis is $0\,\text{mm}$. 15 trials were conducted for each swimmer and controller combination.

To reduce the on-line adaption and convergence process time, the path-following performances of MRAC shown in Fig 6 (a) and (c) are the results after the initial adaption
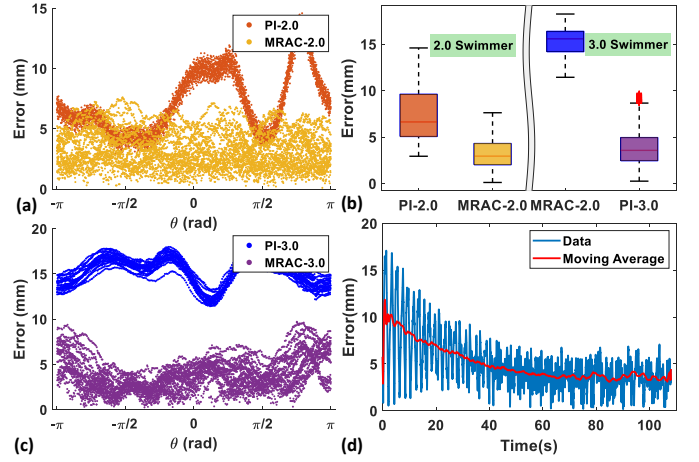

Fig. 6. PI controller vs. MRAC. (a) The path-following error as a function of angle around the circle for a $2\,\text{mm}$ pitch swimmer. (b) The box and whisker plots of each swimmer and controller, and each box and whisker contains 15 trials. (c) The path-following error as a function of angle around the circle for a $3\,\text{mm}$ pitch swimmer. (d) The adaption process of MRAC with the $3\,\text{mm}$ pitch swimmer.

process, and the error is defined as the Euclidean distance between the swimmer position and the closest point on the desired path.

The path-following controller comparison results for a $2\,\text{mm}$ pitch swimmer are shown in Fig. 6 (a). Because the 2.0 Swimmer was more stable than the other swimmers, the curves of both controllers are close to each other. However, the results of MRAC are concentrated in a low band rather than oscillating as with the PI controller. The mean and standard deviation (std) for the PI controller and MRAC are shown in Table II. Compared to the PI controller, the MRAC reduced the mean error by $56.75\,\%$ and the std by $44.44\,\%$, using the 2.0 Swimmer.

The path-following error curves of the $3\,\text{mm}$ pitch swimmer are shown in Fig. 6 (c), and the mean $\pm$ std for the PI controller and MRAC are shown in Table II. As these results show, the MRAC significantly improved the tracking performance of the 3.0 Swimmer. Compared to the PI controller, the MRAC reduced the mean error by $75.0\,\%$. The MRAC path-following performance of both swimmers is within one body length of the swimmer ($6\,\text{mm}$), considering the mean error $\pm$ std. A box and whisker plot comparing these controllers is shown in Fig. 6 (b), which more intuitively shows the performance gap between two controllers. The on-line adaption and convergence process of $3\,\text{mm}$ pitch swimmer starting from the beginning is shown in Fig. 6 (d). The mean error decreased from $10\,\text{mm}$ to $5\,\text{mm}$, and took about $100\,\text{sec}$.

C. Path-Following on Two 3D Trajectories

See attachment for videos of path-following [36]. The 2.0 Swimmer was used to follow a desired helical path using MRAC. The swimmer took off from the tank on the bottom left corner, as shown in Fig. 7 (a), and went through three pairs of $8\,\text{mm}$ holes on the transparent acrylic board with three heights. The swimmer's path-following trajectory is presented in Fig. 7

TABLE I
SWIMMER DESIGNS. ALL SWIMMERS ARE 6 mm LONG AND 2.5 mm IN DIAMETER

Schematic					
Details	1.0 Swimmer Single Helix Pitch: 1 mm	1.5 Swimmer Single Helix Pitch: 1.5 mm	2.0 Swimmer Single Helix Pitch: 2 mm	2.5 Swimmer Single Helix Pitch: 2.5 mm	3.0 Swimmer Single Helix Pitch: 3 mm
Mean	7.1 mm	11.4 mm	7.4 mm	14.5 mm	15.2 mm
Std	3.3 mm	3.7 mm	2.7 mm	1.4 mm	1.5 mm

TABLE II
CONTROLLER COMPARISON

Pitch	2 mm		3 mm	
Controller	PI	MRAC	PI	MRAC
Mean (mm)	7.4	3.2	15.2	3.8
Std (mm)	2.7	1.5	1.5	1.8

(a), which contains 10 trials. The path-following mean error of this case is 4.2 ± 4 mm.

The ability to swim forwards and in reverse enables maneuvering in tight environments. These swimmers have a sharp front and a blunt back end, so swimming forwards requires different control values than swimming backwards. To achieve backward path-following, one additional set of MRAC parameters was implemented in the program, and the body frame W-axis of the swimmer was flipped $180°$ during the backward movement. The forward and backward parameters of MRAC can be switched according to the desired trajectory and movement direction. The forward motion is defined with the helix tip leading as shown in Fig. 7 (c), and the backward motion is defined with the tail leading as shown in Fig. 7 (d). As shown in Fig. 7 (b), the swimmer started from Point A, and moved forward to Point B. Then the swimmer moved backward from Point B to Point A with its tail leading. The forward motion trajectory of the swimmer is plotted in blue, and the backward motion trajectory is plotted in red. The plot shown in Fig. 7 (b) contains 10 trials. The mean error of the forward motion is 2.7 ± 1.6 mm, and the mean error of the backward motion is 3.5 ± 2.0 mm.

IV. CONCLUSIONS AND FUTURE WORK

This paper reports an efficient on-line method to calculate and compensate for the gradient force applied on a rotating magnetic swimmer during 3D guidance. To evaluate the relationship between pitch and stability of the swimmer design, five thread-pitch values were experimentally investigated. A swimmer with a 2.0 mm pitch had the best stability among all designs tested. Additionally, to improve the path-following accuracy of the 3D guidance, a direct model reference adaptive controller (MRAC) was implemented and compared with the PI controller proposed in our previous work. Switching from a PI controller to MRAC significantly improved the path-following performance. The path-following mean error is 3.8 ± 1.8 mm, which is smaller than one body length of
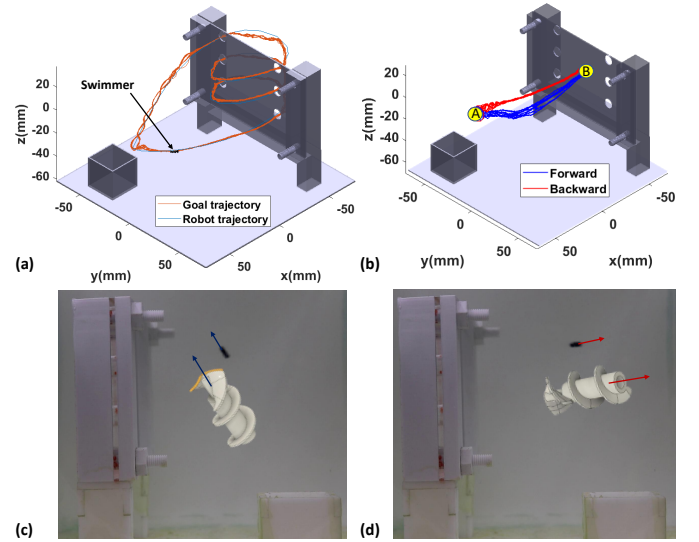

Fig. 7. Path-Following on a Helical Trajectory and Forward & Backward Motion. (a) 10 cycles of path-following on a helical trajectory through six holes, each 8 mm in diameter. (b) 10 cycles of path-following using forward and backward motions. (c) Snapshot during forward motion. (d) Snapshot during backward motion. See video attachment [36], https://youtu.be/U3xE5grzTLc.

the swimmer (6 mm). The path-following performance on a complex trajectory, and forward & backward motion using MRAC were also analyzed.

An L_1 adaptive controller may also improve the path-following in a 3D environment. As analyzed and discussed in [37], an L_1 adaptive controller may provide more stability margin and better disturbance rejection than MRAC.

Future work could study the implementation of sensors to measure the orientation of the permanent magnet in real time. The estimation of the magnet's orientation would improve magnetic gradient compensation and enable closed-loop torque control. An array of Hall effect sensors could be used to estimate the position and orientation of a tetherless magnetic robot [38]. This solution is challenging to implement because the magnetic field produced by the EMs must be subtracted from the measurement to obtain the field produced by the miniature permanent magnet only. The field produced by this permanent magnet decreases rapidly with distance. The magnetic field measured at the location of the probes will be dominated by the field produced by the EMs.

ACKNOWLEDGMENT

REFERENCES

[1] B. J. Nelson, I. K. Kaliakatsos, and J. J. Abbott, "Microrobots for minimally invasive medicine," *Annual review of biomedical engineering*, vol. 12, pp. 55–85, 2010.

[2] S. Tottori, L. Zhang, F. Qiu, K. K. Krawczyk, A. Franco-Obregón, and B. J. Nelson, "Magnetic helical micromachines: fabrication, controlled swimming, and cargo transport," *Advanced materials*, vol. 24, no. 6, pp. 811–816, 2012.

[3] K. E. Peyer, L. Zhang, and B. J. Nelson, "Bio-inspired magnetic swimming microrobots for biomedical applications," *Nanoscale*, vol. 5, no. 4, pp. 1259–1272, 2013.

[4] F. Qiu and B. J. Nelson, "Magnetic helical micro-and nanorobots: Toward their biomedical applications," *Engineering*, vol. 1, no. 1, pp. 021–026, 2015.

[5] H. C. Berg and R. A. Anderson, "Bacteria swim by rotating their flagellar filaments," *Nature*, vol. 245, no. 5425, p. 380, 1973.

[6] E. M. Purcell, "Life at low reynolds number," *American journal of physics*, vol. 45, no. 1, pp. 3–11, 1977.

[7] T. Honda, K. Arai, and K. Ishiyama, "Micro swimming mechanisms propelled by external magnetic fields," *IEEE Transactions on Magnetics*, vol. 32, no. 5, pp. 5085–5087, 1996.

[8] K. E. Peyer, S. Tottori, F. Qiu, L. Zhang, and B. J. Nelson, "Magnetic helical micromachines," *Chemistry–A European Journal*, vol. 19, no. 1, pp. 28–38, 2013.

[9] T. Xu, J. Yu, X. Yan, H. Choi, and L. Zhang, "Magnetic actuation based motion control for microrobots: An overview," *Micromachines*, vol. 6, no. 9, pp. 1346–1364, 2015.

[10] A. W. Mahoney, J. C. Sarrazin, E. Bamberg, and J. J. Abbott, "Velocity control with gravity compensation for magnetic helical microswimmers," *Advanced Robotics*, vol. 25, no. 8, pp. 1007–1028, 2011.

[11] M. E. Alshafeei, A. Hosney, A. Klingner, S. Misra, and I. S. Khalil, "Magnetic-based motion control of a helical robot using two synchronized rotating dipole fields," in *5th IEEE RAS/EMBS International Conference on Biomedical Robotics and Biomechatronics*. IEEE, 2014, pp. 151–156.

[12] T. Xu, Y. Guan, J. Liu, and X. Wu, "Image-based visual servoing of helical microswimmers for planar path following," *IEEE Transactions on Automation Science and Engineering*, 2019.

[13] K. Yoshida and H. Onoe, "Soft spiral-shaped micro-swimmer with propulsion force control by pitch change," in *2019 20th International Conference on Solid-State Sensors, Actuators and Microsystems & Eurosensors XXXIII (TRANSDUCERS & EUROSENSORS XXXIII)*. IEEE, 2019, pp. 217–220.

[14] T. Xu, G. Hwang, N. Andreff, and S. Régnier, "Planar path following of 3-d steering scaled-up helical microswimmers," *IEEE Transactions on Robotics*, vol. 31, no. 1, pp. 117–127, 2015.

[15] A. Oulmas, N. Andreff, and S. Régnier, "Closed-loop 3d path following of scaled-up helical microswimmers," in *2016 IEEE International Conference on Robotics and Automation (ICRA)*. IEEE, 2016, pp. 1725–1730.

[16] X. Wu, J. Liu, C. Huang, M. Su, and T. Xu, "3-d path following of helical microswimmers with an adaptive orientation compensation model," *IEEE Transactions on Automation Science and Engineering*, 2019.

[17] J. Leclerc, B. Isichei, and A. T. Becker, "A magnetic manipulator cooled with liquid nitrogen," *IEEE Robotics and Automation Letters*, vol. 3, no. 4, pp. 4367–4374, 2018.

[18] A. J. Petruska and B. J. Nelson, "Minimum bounds on the number of electromagnets required for remote magnetic manipulation," *IEEE Transactions on Robotics*, vol. 31, no. 3, pp. 714–722, 2015.

[19] J. Van Bladel and J. Van Bladel, *Singular electromagnetic fields and sources*. Clarendon Press Oxford, 1991.

[20] T. W. Fountain, P. V. Kailat, and J. J. Abbott, "Wireless control of magnetic helical microrobots using a rotating-permanent-magnet manipulator," in *2010 IEEE International Conference on Robotics and Automation*. IEEE, 2010, pp. 576–581.

[21] A. W. Mahoney and J. J. Abbott, "Managing magnetic force applied to a magnetic device by a rotating dipole field," *Applied Physics Letters*, vol. 99, no. 13, p. 134103, 2011.

[22] M. P. Kummer, J. J. Abbott, B. E. Kratochvil, R. Borer, A. Sengul, and B. J. Nelson, "Octomag: An electromagnetic system for 5-dof wireless micromanipulation," *IEEE Transactions on Robotics*, vol. 26, no. 6, pp. 1006–1017, 2010.

[23] L. Yang, X. Du, E. Yu, D. Jin, and L. Zhang, "Deltamag: An electromagnetic manipulation system with parallel mobile coils," in *2019 International Conference on Robotics and Automation (ICRA)*. IEEE, 2019, pp. 9814–9820.

[24] K. Ishiyama, M. Sendoh, A. Yamazaki, and K. Arai, "Swimming micromachine driven by magnetic torque," *Sensors and Actuators A: Physical*, vol. 91, no. 1-2, pp. 141–144, 2001.

[25] K. Ishiyama, K. Arai, M. Sendoh, and A. Yamazaki, "Spiral-type micromachine for medical applications," in *MHS2000. Proceedings of 2000 International Symposium on Micromechatronics and Human Science (Cat. No. 00TH8530)*. IEEE, 2000, pp. 65–69.

[26] K. Ishiyama, M. Sendoh, and K. Arai, "Magnetic micromachines for medical applications," *Journal of Magnetism and Magnetic Materials*, vol. 242, pp. 41–46, 2002.

[27] H. Zhou, G. Alici, T. D. Than, and W. Li, "Modeling and experimental characterization of propulsion of a spiral-type microrobot for medical use in gastrointestinal tract," *IEEE Transactions on Biomedical engineering*, vol. 60, no. 6, pp. 1751–1759, 2012.

[28] J. Leclerc, Z. Haoran, and A. T. Becker, "3d control of rotating millimeter-scale swimmers through obstacles," *IEEE International Conference on Robotics and Automation*, p. forthcoming, 2019.

[29] J. C. Simpson, J. E. Lane, C. D. Immer, and R. C. Youngquist, "Simple analytic expressions for the magnetic field of a circular current loop," NASA, Kennedy Space Center, Florida, Tech. Rep., 2001. [Online]. Available: https://ntrs.nasa.gov/archive/nasa/casi.ntrs.nasa.gov/20140002333.pdf

[30] A. N. Tikhonov, A. Goncharsky, V. Stepanov, and A. G. Yagola, *Numerical methods for the solution of ill-posed problems*. Springer Science & Business Media, 2013, vol. 328.

[31] H. Kaufman, I. Barkana, and K. Sobel, *Direct adaptive control algorithms: theory and applications*. Springer Science & Business Media, 2012.

[32] D. Zhang and B. Wei, "Convergence performance comparisons of pid, mrac, and pid+ mrac hybrid controller," *Frontiers of Mechanical Engineering*, vol. 11, no. 2, pp. 213–217, 2016.

[33] S. Xiao, Y. Li, and J. Liu, "A model reference adaptive pid control for electromagnetic actuated micro-positioning stage," in *2012 IEEE International Conference on Automation Science and Engineering (CASE)*. IEEE, 2012, pp. 97–102.

[34] P. Jain and M. Nigam, "Design of a model reference adaptive controller using modified mit rule for a second order system," *Advance in Electronic and Electric Engineering*, vol. 3, no. 4, pp. 477–484, 2013.

[35] T. Yucelen, "Model reference adaptive control," *Wiley Encyclopedia of Electrical and Electronics Engineering*, pp. 1–13, 2019.

[36] H. Zhao, J. Leclerc, and A. T. Becker, "3d path-following using a millimeter-scale magnetic robot," 2020. [Online]. Available: https://youtu.be/U3xE5grzTLc

[37] E. Kharisov, N. Hovakimyan, and K. strm, "Comparison of several adaptive controllers according to their robustness metrics," in *AIAA Guidance, Navigation, and Control Conference*, 2012. [Online]. Available: https://arc.aiaa.org/doi/abs/10.2514/6.2010-8047

[38] D. Son, S. Yim, and M. Sitti, "A 5-d localization method for a magnetically manipulated untethered robot using a 2-d array of hall-effect sensors," *IEEE/ASME Transactions on Mechatronics*, vol. 21, no. 2, pp. 708–716, 2015.